Nanoscale

PAPER

View Article Online
View Journal | View Issue

Cite this: *Nanoscale*, 2015, **7**, 1849

Bimodal frequency-modulated atomic force microscopy with small cantilevers†

Christian Dietz,*[a,b] Marcus Schulze,[a,b] Agnieszka Voss,[a,b] Christian Riesch[c] and Robert W. Stark*[a,b]

Received 8th October 2014,
Accepted 10th December 2014

DOI: 10.1039/c4nr05907g

www.rsc.org/nanoscale

Small cantilevers with ultra-high resonant frequencies (1–3 MHz) have paved the way for high-speed atomic force microscopy. However, their potential for multi-frequency atomic force microscopy is unexplored. Because small cantilevers have small spring constants but large resonant frequencies, they are well-suited for the characterisation of delicate specimens with high imaging rates. We demonstrate their imaging capabilities in a bimodal frequency modulation mode in constant excitation on semi-crystalline polypropylene. The first two flexural modes of the cantilever were simultaneously excited. The detected frequency shift of the first eigenmode was held constant for topographical feedback, whereas the second eigenmode frequency shift was used to map the local properties of the specimen. High-resolution images were acquired depicting crystalline lamellae of approximately 12 nm in width. Additionally, dynamic force curves revealed that the contrast originated from different interaction forces between the tip and the distinct polymer regions. The technique uses gentle forces during scanning and quantified the elastic moduli E_{am} = 300 MPa and E_{cr} = 600 MPa on amorphous and crystalline regions, respectively. Thus, multimode measurements with small cantilevers allow one to map material properties on the nanoscale at high resolutions and increase the force sensitivity compared with standard cantilevers.

Introduction

To understand the functionality of complex materials, it is essential to map the local distribution of the components and material properties on a microscopic scale. To this end, the atomic force microscope (AFM) is a reliable tool which allows one to map heterogeneous surfaces at the nanoscale with respect to elasticity, viscosity or deformability. Dynamic AFM methods[1–3] enable the simultaneous determination of both elastic and dissipative, and hence, velocity-dependent, interactions between a sharp tip and the sample surface. For resonant measurements in amplitude or frequency modulations, stiff cantilevers (with spring constants of 10 N m^{-1} to 50 N m^{-1}) with relatively low resonant frequencies (100 kHz to 400 kHz) are typically used. However, with monomodal cantilever excitation, the minimum detectable force gradient of the sensor increases with increasing stiffness k_1 but decreases with an increasing resonant frequency of the fundamental mode f_{01}:[4]

$$\partial F'_{\min} = \sqrt{k_1 k_B T B / \pi f_{01} Q_1 \langle A_1^2 \rangle}, \quad (1)$$

where k_BT is the thermal energy of the particular medium, B is the measurement bandwidth, Q is the quality factor of the oscillating cantilever, and $\langle A_1^2 \rangle$ is the mean-squared amplitude of the fundamental eigenmode. In contrast, commercially available small cantilevers that are characterised by their very small plane-view dimensions and low thickness[5,6] are typically much softer (with spring constants of 1 N m^{-1} to 10 N m^{-1}) and feature resonant frequencies an order of magnitude higher (1 MHz to 3 MHz) than conventional ones. Hence, they offer more gentle imaging conditions and higher lateral resolution and allows for faster imaging due to an improved time response. An additional advantage of small cantilevers is a reduced deflection noise density because the thermal energy k_BT is distributed over a wider frequency range as compared to conventional cantilevers. Consequently, the signal-to-noise-ratio for imaging is enhanced during oscillation. A breakthrough application of these sensors has already been demonstrated in amplitude modulation AFM using high scan velocities, also known as high-speed AFM,[7–12] and has had a tremendous impact in the biological sciences.[13,14] Recently, Fukuma *et al.*[15] succeeded in achieving the atomic resolution of mica in liquid using small cantilevers for frequency

[a]*Center of Smart Interfaces, Technische Universität Darmstadt, Alarich-Weiss-Str. 10, 64287 Darmstadt, Germany*
[b]*Physics of Surfaces, Institute of Materials Science, Technische Universität Darmstadt, Alarich-Weiss-Str. 16, 64287 Darmstadt, Germany. E-mail: dietz@csi.tu-darmstadt.de, stark@csi.tu-darmstadt.de*
[c]*Chemische Physik, Technische Universität Chemnitz, Reichenhainer Str. 70, 09126 Chemnitz, Germany*
† Electronic supplementary information (ESI) available. See DOI: 10.1039/c4nr05907g

modulation AFM and confirmed the lower minimum detectable force gradient due to higher resonant frequencies of these probes compared with conventional "long" cantilevers. However, the advantages of small cantilevers for multi-frequency imaging, are not yet fully realised because of the limited capabilities for detection electronics to accommodate the high bandwidth of the sensors.

The analysis of higher harmonics and eigenmodes of the cantilever[16] allows one to enhance the lateral imaging resolution,[17,18] the sensitivity[19–21] or to reconstruct and map nonlinear tip-sample interactions.[22–25] Multi-frequency AFM implies the simultaneous excitation and detection of the AFM signal at various frequencies in order to map and quantitatively determine surface properties.[26–31] Rodriguez and Garcia[32] suggested the use of the first two flexural eigenmodes in amplitude modulation AFM. Later, this approach was extended to a frequency modulation in a constant amplitude mode with the ability to map the local elasticity, viscosity and deformation in air[33] and the elasticity in liquids.[34]

In this study, we demonstrate high-resolution, bimodal frequency modulation AFM[4,33,35–37] imaging with constant excitation (CA-FM-FM-AFM) using small cantilevers on a heterogeneous polymer surface consisting of stiff crystals embedded in a soft amorphous matrix. While the first two flexural eigenmodes of the cantilever are simultaneously excited with constant driving amplitudes, the deflection signal of the photodiode is analysed by two independent phase-locked-loop circuits. This allows for the tracking of instantaneous amplitudes and frequency shifts of both eigenmodes due to the tip-sample interaction (Fig. 1). Two phase shifters assure that the cantilever is permanently excited at the two resonances. Additionally, a proportional-integral feedback loop varies the tip-sample distance in such a way that the frequency shift of the first eigenmode oscillation is kept at a constant value during imaging. In general, frequency modulation atomic force microscopy enables the operator to transform the observables into quantitative data. In the constant excitation mode, the force acting between the tip and the sample surface can be correlated with the frequency shift of the first eigenmode Δf_1 and the respective oscillation amplitude A_1 using a formula developed by Holscher *et al.*:[38,39]

$$F(D) \cong \sqrt{2}\frac{\partial}{\partial D}\int_D^\infty \frac{k_1 {A_1}^{3/2}}{f_{01}}\frac{\Delta f_1(z')}{\sqrt{z'-D}}\mathrm{d}z', \quad (2)$$

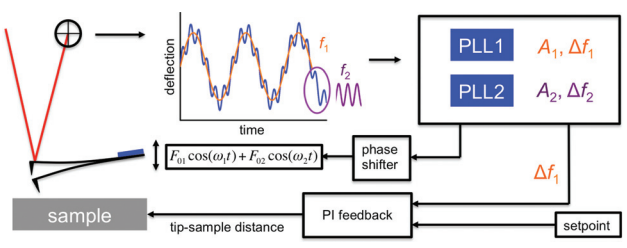

Fig. 1 Principle of bimodal frequency-modulated atomic force microscopy with constant excitation.

where k_1 is the cantilever force constant, f_{01} is the first eigenmode resonant frequency of the undisturbed oscillation, D is the minimum tip-sample distance, and $z' = z + D + A_1$ is the scaling of the instantaneous tip position.[38] Assuming that the energy dissipated between tip and sample can be treated independently for each eigenmode, we obtain the total dissipated energy $E_{\mathrm{dis,tot}}$ as the sum:

$$E_{\mathrm{dis,tot}} \cong \pi \sum_{i=1}^{N} k_i \left(A_i a_{i,\mathrm{exc}} - \frac{{A_i}^2}{Q_i} \right). \quad (3)$$

Here, k_i, A_i, $a_{i,\mathrm{exc}}$ Q_i are the force constant, oscillation amplitude, excitation amplitude and the quality factor of the eigenmode i. N is the total number of excited eigenmodes.

In the constant amplitude mode, Herruzo *et al.*[37] demonstrated that the frequency shift of the first eigenmode is a direct measure of the half integral of the force between tip and sample, whereas the frequency shift of the second eigenmode varies with the half derivative of the tip-sample force. Assuming a Hertzian contact mechanics and a linear viscous model, both observables Δf_1 and Δf_2 are sufficient for the quantification of the local elastic modulus of the sample surface under the condition that the free first eigenmode amplitude is much larger than the second one:[33]

$$E_{\mathrm{eff}} = \sqrt{\frac{8}{RA_1}}\frac{{k_2}^2}{k_1}\frac{f_{01}}{{f_{02}}^2}\frac{{\Delta f_2}^2}{\Delta f_1}, \quad (4)$$

where R is the tip radius, k_1 and k_2, f_{01} and f_{02}, and Δf_1, and Δf_2 are force constants, free vibration resonance frequencies and their shifts pertaining to both eigenmodes, respectively. In this paper, we demonstrate that applying Holscher's formula[38,39] is a reasonable method for bimodal FM-FM-AFM in constant excitation mode to estimate the force acting between the tip and a polymer that is both crystalline and amorphous. Furthermore, we show that eqn (4) can be used to transform the frequency shifts of both eigenmodes into the local mechanical stiffness of a sample.

Experimental section

Bimodal frequency modulation atomic force microscopy in constant excitation mode

We extended a commercially available atomic force microscope (Cypher, Asylum Research, Santa Barbara, USA) with a dual phase locked loop device (HF2PLL, Zurich Instruments AG, Zurich, Switzerland) to simultaneously track frequency shifts of the first two flexural eigenmodes of the cantilever when the tip interacts with a sample. Gentle imaging was guaranteed by limiting the scan speed to 540 nm s^{-1} and adjusting the set point frequency of the first eigenmode no higher than Δf = −60 Hz leading to an operation of the microscope in a net attractive regime. The scan velocity and the frequency setpoint were balanced to obtain a good second eigenmode frequency-contrast between the two polymer components in the attractive operation regime while scanning at reasonable scan rates.

A low contrast in the image of the first eigenmode frequency-shift signalized a properly functioning feedback-loop implying low forces and gentle imaging conditions. The second eigenmode was free to sense different mechanical forces acting on the tip.

To enhance the sensitivity and minimise the thermal noise of the instrument, we applied ultra-high frequency small cantilevers (Arrow™ UHF, Nanoworld, Neuchâtel, Switzerland) with flexural resonance frequencies of f_1 = 1.4–2.0 MHz and f_2 = 4.8–6.0 MHz of the first and second eigenmodes, respectively. Force constants k_1 = 3 N m^{-1} and $k_2 \approx$ 313 N m^{-1} were determined by the thermal noise method.[40] We note that the determination of the second eigenmode force constant with the thermal noise method can have larger errors than the determination of the first eigenmode.[41] Thus, the absolute values for the elasticity should be interpreted with due caution. To estimate the oscillation amplitudes of both eigenmodes, we measured the optical lever sensitivity by approaching the cantilever (static mode, *i.e.* dither-piezo off) towards a stiff silicon surface and recording the deflection signal of the photodiode [V] *versus* separation [nm] dependency. From the inverse slope, we obtained the static sensitivity σ_s = 30 nm V^{-1}. We deduced the dynamic sensitivities of the *n*-th eigenmode, taking advantage of the relationship between optical sensitivities and cantilever slopes,[42,43] leading to the dynamic sensitivities σ_1 = 33 nm V^{-1} and σ_2 = 9 nm V^{-1}. Scanning was performed in a constant excitation mode driving the free amplitudes to approximately $A_{01} \approx$ 23 nm and $A_{02} \approx$ 2 nm. Amplitude reductions of approximately 23% for both eigenmodes during imaging caused by elastic forces and viscous damping were detected. The relatively large free amplitude of the first eigenmode guaranteed a stable oscillation of the small cantilevers with a low stiffness on the viscous polymer. Similar experiments performed with conventional "long" cantilevers, *e.g.* PPP-FM (Nanoworld, Neuchâtel, Switzerland) with similar force constants of k = 1–3 N m^{-1} and free amplitudes resulted in "snap-into-contact" during the approach. The amplitude broke down drastically (amplitude reduction to approximately 10%) and thus stable imaging was impossible.

Material and sample preparation

A 300 nm-thick film of elastomeric polypropylene with a weight-average molecular weight of M_w = 160 kg mol^{-1} and a [*mmmm*]-pentade (*m* = *meso* conformation) content of 22% was prepared by drop casting 5 mg mL^{-1} of the polymer in decaline onto a silicon (100) substrate. After the evaporation of the decaline, we removed the top layer (approximately 33 nm thick) following the protocol established by Rehse *et al.*[44] by successively wet-chemical etching three times with 1 mg potassium permanganate in 20 mL 30 wt% sulphuric acid. After each etching step, the polymer surface was flushed with 10 wt% sulphuric acid, then hydrogen peroxide, water and acetone. Finally, the specimen was blown dry with nitrogen.

Image post processing

Images were first order flattened to remove global sample tilt.

Results and discussion

Imaging

The imaging capability of CA-FM-FM AFM is shown in Fig. 2. Images of an elastomeric polymer sample consisting of a mixture of stiff crystalline and soft amorphous polypropylene were captured. The enrichment of the amorphous polymer on the surface of the as-prepared sample is a well-known phenomenon.[18,45–47] For this reason, we removed approximately 20 nm of the top layer by wet-chemical etching as described in the experimental section. To ensure a stable oscillation of the cantilever particularly on the viscoelastic amorphous regions, a relatively high free vibration amplitude of approximately 23 nm for the first eigenmode was chosen, while the second eigenmode free amplitude was approximately 2 nm. The surface root mean squared roughness in the topography image (Fig. 2a, scan size: 650 × 650 nm^2) was determined to 4 nm.

The tips of the crystals slightly protrude from the amorphous matrix but the complete crystalline structure cannot be resolved in the topography image. The image of the frequency shift corresponding to the first eigenmode oscillation (Fig. 2b) was extremely smooth, depicting deviations of only 2 Hz from the set point value. This suggests a high accuracy of the main feedback loop running on that mode for the topography acquisition at a constant tip-sample force. In contrast, the second eigenmode frequency shift image (Fig. 2c) explicitly resolved the crystalline structure within the amorphous matrix. The bright lamellae correspond to crystals ($\Delta f_2 \approx$ 290 Hz); the dark matrix correspond to the polymer in the amorphous state

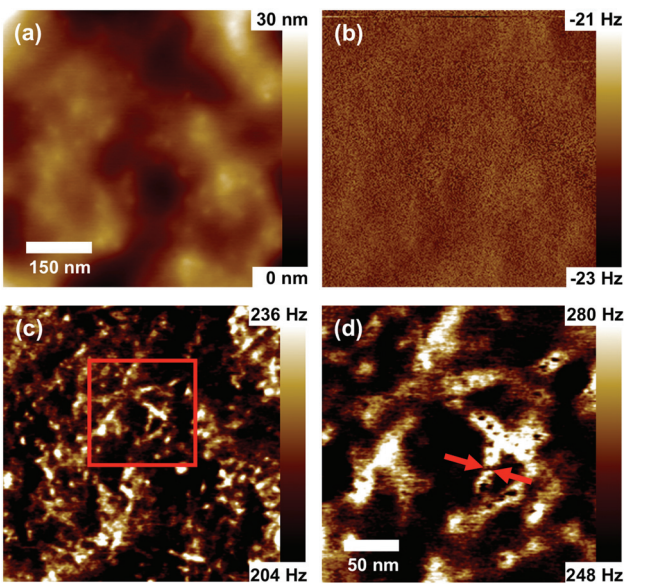

Fig. 2 Bimodal CA-FM-FM AFM images of elastomeric polypropylene. (a) Topography image, (b) first eigenmode frequency shift image and (c) second eigenmode frequency shift image depicting the local distribution of crystalline polypropylene within the amorphous matrix. (d) Enlarged rescan of the red framed region of (c). The crystal highlighted by the red arrows depicts a width of approximately 12 nm.

($\Delta f_2 \approx 220$ Hz). Fig. 2d shows a magnified rescan of the polymer structure of the red framed area in Fig. 2c. From the cross section of a single crystalline lamella (indicated by red arrows), we estimated a lateral resolution of approximately 12 nm. At several positions, dark spots in the middle of crystalline lamellae are visible whose origin is not yet clear. These spots persisted after repeated scans. We tentatively attribute these spots to local defects of the crystalline structure. Increasing the tip speed led to a reduced contrast between crystalline lamellae and amorphous regions in the second eigenmode frequency-shift image. In a benchmark experiment (see ESI, Fig. S1 and S2†), we could demonstrate that the polymer structure was resolvable at tip velocities v_{tip} up to 3.3 μm s^{-1} and the topography could be properly traced even at v_{tip} = 6.5 μm s^{-1} although ringing was evident in the Δf_1 data (imaging time of 20 s, scan size 500 × 500 nm^2, resolution 256 × 256 pixel). Although the imaging parameters were not yet fully optimized, these examples illustrate the potential to speed up bimodal FM-FM atomic force microscopy in constant excitation mode.

Spectroscopy

Dynamic force-*versus*-distance experiments were conducted on single crystals and on amorphous polypropylene to understand the contrast mechanism, to estimate the indentation of the tip into the sample surface, and to calculate the elasticity, dissipation and interaction forces. We recorded the amplitudes and frequency shifts of both eigenmodes A_1, A_2, Δf_1, Δf_2 as functions of the *z*-piezo position by varying the mean tip-sample distance. Fig. 3a shows a typical amplitude-*versus*-*z*-piezo position of the first eigenmode. The oscillating tip approached the sample surface on a crystalline region (red line) and on an amorphous region (black line), while a free second eigenmode amplitude of 1.8 nm was simultaneously excited. Higher or lower driven A_{02} did not considerably affect the shape of these curves. From the onset of the interactions between the tip and sample (z = 0 nm) until a *z*-piezo position of approximately −6 nm was reached, both curves exhibited an almost linear decrease with a slope $\partial A_1/\partial z \approx 1$, *i.e.*, the slope of an infinitely stiff sample surface (indicated by a dashed grey line). For *z*-values smaller than −6 nm, both curves decreased more rapidly with smaller values for the crystalline region. Corresponding second eigenmode amplitudes *versus* *z*-piezo positions measured for three different free amplitudes (A_{02} = 0.8 nm, 1.8 nm, and 5.5 nm) can be seen in the inset of the same figure. All amplitude curves depend on the *z*-piezo position in a highly non-linear fashion. The respective frequency shifts for the second eigenmode recorded on the crystalline regions (red curve) and on the amorphous polymer (black curve) can be taken from the graph in Fig. 3b. The frequency shifts for both polymer regions are mainly positive with higher values on the crystalline region and negative values between z = −2.2 nm and z = 0 nm with a minimum value of −20 Hz at z = −1.3 nm. When the feedback operates the *z*-piezo in the regime highlighted by the grey box in the inset of Fig. 3b we obtain the contrast visible in the images of the second eigenmode frequency shift of Fig. 2(c) and (d).

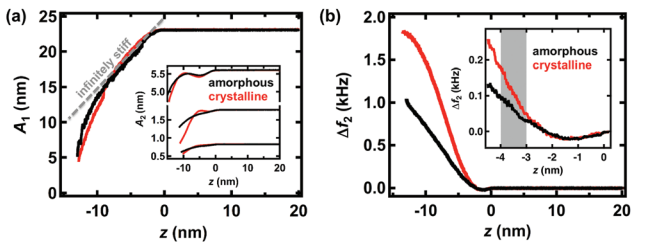

Fig. 3 (a) First eigenmode amplitude *versus* *z*-piezo position measured on crystalline (red) and amorphous regions (black). The grey dashed line indicates the amplitude decrease of an infinitely stiff sample. The inset shows the second eigenmode amplitude decrease *versus* *z*-piezo position for three different free amplitudes. (b) Frequency shift *versus* *z*-piezo position for the second eigenmode measured on crystalline (red) and amorphous (black) regions. The grey box in the inset highlights the *z*-piezo regime for which the difference between the frequency shifts obtained on crystalline and amorphous regions matches the contrast acquired in Fig. 2(c) and (d).

In the case of monomodal excitation, a sample which shows a linear decrease of the amplitude-*versus*-*z*-piezo position with a slope $\partial A_1/\partial z$ = 1 can be interpreted as infinitely stiff, *i.e.*, having no indentation of the tip into the sample surface. In a bimodal excitation experiment, there is an additional oscillation superimposed on the first eigenmode movement of the cantilever. The second eigenmode amplitude depends non-linearly on the *z*-piezo position. However, because the change in amplitude is small (<0.2 nm) for a wide *z*-piezo range (up to z = −6 nm after the tip begins to interact with the sample surface), in particular for the experimental conditions used in this study (A_{02} = 2 nm, Fig. 2), we conclude that the additional oscillation penetrates through the sample surface unaffected, leading to indentation depths corresponding to the free amplitudes of the second eigenmode. This behaviour can be observed on both polymer regions making them indistinguishable with respect to the indentation.

We also investigated the influence of the second eigenmode oscillation on the first eigenmode frequency shift. Different constant excitation forces were applied to vary the free second eigenmode vibration amplitude for $A_{02} \in$ [0 nm, 0.8 nm, 1.8 nm, 5.5 nm]; the first eigenmode amplitude was set to a constant 23 nm in a free vibration state ($z \approx 3$ μm above the sample surface). By approaching the surface with the cantilever, the frequency shift of the first eigenmode was recorded on amorphous (Fig. 4a) and crystalline polypropylene (Fig. 4b). On the amorphous region, frequency shifts in the negative values were obtained during the whole approach. A minimum value was observed at z = −10 nm for free second eigenmode amplitudes of A_{02} = 0 nm–1.8 nm. Minor differences were found in the minimum frequency, ranging from −1.5 kHz to −1.3 kHz. The greater the A_{02}, the more the minimum frequency shifts to greater values. For A_{02} = 5.5 nm, a transition from negative to positive frequency shifts with respect to the free resonant frequency occurred at z = −11 nm. Here, the curve significantly differed from those of the low second eigenmode driving forces. On crystalline regions, the first

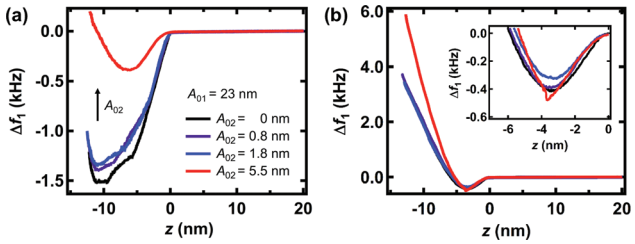

Fig. 4 First eigenmode frequency shift *versus* *z*-piezo position for different free amplitudes of the second mode obtained on amorphous (a) and crystalline regions (b). The inset in (b) enlarges the negative frequency shift regime.

eigenmode resonant frequencies first shifted to negative values until $z = -6$ nm. On the continued approach of the cantilever towards the sample surface, a shift to positive values was observed. The curves for low A_{02} ($\leq$1.8 nm) coincided with slight differences in the minimum frequency shift at $z = -3.3$ nm and resulted in greater minima for greater A_{02} (*cf.* inset Fig. 4b). The curve for the high amplitude A_{02} = 5.5 nm showed significantly higher frequency shifts for $z < -6$ nm compared with the low amplitude cases.

These results demonstrate predominantly attractive interactions during one oscillation cycle of the tip with amorphous regions for the monomodal case and for moderate second eigenmode excitation forces. However, on the crystalline areas, the interaction forces can become repulsive when moving the cantilever close to the surface. For low second eigenmode free amplitudes, *i.e.*, $\leq$8% of the free oscillation amplitude of the first eigenmode, there were few interactions between the two oscillation states because the recorded frequency shifts were very close to the monomodal case. These observations justify the utilisation of eqn (2) to estimate average forces between the oscillating tip and the sample surface during scanning. We emphasise that eqn (2) considered only the frequency shift of the first eigenmode and ignored the presence of an additional oscillation. However, this assumption should introduce only small errors to the total force because of the negligible interference between both modes. For the experimental conditions employed for imaging (see Fig. 2, A_{01} = 23.5 nm and A_{02} = 1.8 nm), the calculated average forces at each *z*-piezo position derived from the dynamic force measurements on crystalline (red diamonds) and amorphous (black circles) polymer regions are shown in Fig. 5a. When the oscillating tip approached the amorphous region, net attractive forces dominated the interaction over the complete *z*-range with a minimum force value of approximately $F_{min,am} = -100$ pN. On crystalline regions, however, a transition from net attractive to net repulsive forces was observed at $z = -6$ nm with a lowest value of approximately $F_{min,cr} = -30$ pN. These numbers were rather high but do not reflect actual forces during imaging.

The overall forces during imaging can be determined in a straightforward manner: the calculated force curve is compared with the frequency shift data. By interpolating the force data and extracting the values at the *z*-piezo positions where the frequency shift is $\Delta f_1 = -22$ Hz, we obtain $|F| < 10$ pN for both polymer regions. This demonstrates that imaging in this mode is gentle compared with other dynamic imaging techniques, especially on heterogeneous polymers consisting of soft, viscous parts in a stiff, crystalline network. The low force applied to the sample surface is due to the inherently low stiffness of only $k_1 = 3$ N m^{-1} of the small cantilevers used in this study. We would like to emphasize that for fast scan rates these low forces cannot be maintained due to the limitations of the feedback loop. Moreover, forces calculated with eqn (2) are weighted forces. The peak forces are higher.

Eqn (3) allows for the estimation of the non-conservative interactions between the tip and the surface. In Fig. 5b we transformed the amplitude *versus* *z*-piezo position (*cf.* Fig. 3a) into the total energy dissipated per oscillation cycle on the crystalline (red line) and amorphous regions (black line). The inset shows the dissipated energy split up according to the contributions of each eigenmode. After the first interaction between the tip and sample surface, the total dissipated

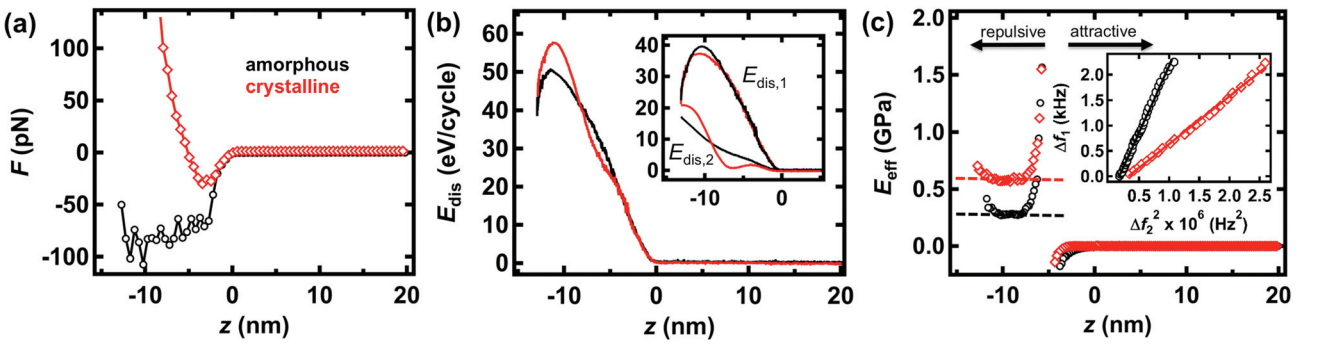

Fig. 5 (a) Force reconstruction according to eqn (2) on amorphous (black circles) and crystalline (red diamonds) polymer regions for A_{01} = 23.5 nm and A_{02} = 1.8 nm (constant excitation mode, approach direction). (b) Total dissipated energy per oscillation cycle on crystalline (red line) and amorphous (black line) polymer regions. The inset displays the contributions of the first ($E_{dis,1}$ – upper curves) and the second ($E_{dis,2}$ – lower curves) eigenmodes. (c) Extracted elastic moduli according to eqn (4) of amorphous (black circles) and crystalline regions (red diamonds) for different *z*-piezo positions (A_{01} = 23.5 nm and A_{02} = 5.5 nm). The arrows indicate the transition from attractive to repulsive interaction regimes. The inset shows the linear dependence of the first eigenmode frequency shift on the square root of the second eigenmode frequency shift verifying the validity of eqn (4).

energy increases with decreasing z-piezo position by the same amount for crystalline and amorphous regions. At $z \approx -6$ nm, *i.e.* where the net tip-sample force becomes overall repulsive, the energy dissipated on the amorphous polymer exceeds the one measured on crystalline regions, whereas for $z < -9$ nm an intersection between the two lines is observable. Both curves have a maximum at $z \approx -11$ nm with a total dissipation of 58 eV and 50 eV on crystalline and amorphous regions, respectively. As can be seen from the inset of Fig. 5b, the intersection of both curves correlates with the energy dissipated in the second eigenmode. The dissipation in the second eigenmodes shows strong non-linear dependencies on the z-piezo position, which is in contrast to the first eigenmodes. Owing to the viscoelastic nature of the polymer in the amorphous region, the energy dissipation is expected to be higher than on the crystalline region.[48] This is observed once the repulsive regime is reached (Fig. 5b). Upon further approach the total energy dissipation on crystalline polypropylene gains a large contribution from the second eigenmode. Considerations of the tip indentation gave rise to the assumption that the second eigenmode cantilever-tip motion penetrated the sample surface nearly unaffectedly. The average forces on the crystals are strong for $z \leq -10$ nm as compared to those on amorphous polypropylene. Most presumably, the repulsive forces push the crystallites into the soft polymer matrix as a whole rather than the tip indenting more than one nanometer into the stiff material.

As recently demonstrated by Herruzo *et al.*, in addition to the forces that can be extracted from bimodal CA-FM-FM-AFM spectroscopy, the stiffness of the sample is quantifiable in terms of the elastic modulus.[33] Because eqn (4) provides a mechanism $\Delta f_1 = \alpha(E_{\text{eff}}, R)\Delta f_2^2$ to validate the spectroscopy data for extracting the elastic modulus, the linearity between Δf_1 and Δf_2^2 is applicable for the data set. The relationship between the frequency shifts of both eigenmodes measured on crystalline (red open diamonds) and amorphous (black open circles) areas of the sample surface is illustrated in the inset of Fig. 5c. Linear regressions calculated for the data points obtained on both polymer states indicate the predicted linear dependency between Δf_1 and Δf_2^2. Furthermore, Fig. 5c shows the effective stiffness *versus* z-piezo position derived from eqn (4). To ensure a transition to the net repulsive regime, the free amplitude of the second eigenmode was excited to A_{02} = 5.5 nm on amorphous regions, while on crystalline regions, A_{02} = 1.8 nm was sufficient.

The graph can be divided into two distinct regions: (1) $z > -6$ nm represents the attractive interaction regime comprising the z-piezo range where no mechanical interaction between the oscillating tip and the sample surface occurs (hence, this range is not suitable for the measurement of the elastic modulus); and (2) $z < -6$ nm, where Pauli repulsion overcomes the attractive van der Waals forces, *i.e.*, the tip apex is pushed into the sample surface. The overall repulsive interaction forms the basis to apply the Hertz contact mechanism in combination with a viscous damping to model the elasticity. Over a wide z-piezo range (*i.e.*, -12 nm $< z < -8$ nm), eqn (4) provides nearly constant elasticity values for both types of polymer states reflecting a setpoint-independent determination of the elastic modulus in the repulsive regime:[33] $E_{\text{eff,am}} \approx 300$ MPa on amorphous areas and $E_{\text{eff,cr}} \approx 600$ MPa on crystalline areas. Close to the transition between the attractive and the repulsive regime, the indentation depth is not sufficient to reliably sense the elasticity (-8 nm $< z < -6$ nm). Deep in the repulsive regime, the applied forces are so strong that the tip motion is not necessarily periodic ($z < -12$ nm). These two regimes define the limits for the validity of eqn (4) for these particular experimental parameters on this specimen. Interestingly, the elasticity values obtained within the range of -12 nm $< z < -8$ nm are in excellent agreement with the values reported using Peak-Force Quantitative Nanomechanical Property Mapping obtained on the same type of polymer.[47] This corroborates the applicability of eqn (4) for bimodal FM-FM AFM performed in a constant excitation mode.

The elasticity value obtained on the amorphous region was nearly the same as the value reported by Gracias *et al.*[49] Initially, the stiffness of the crystal appears low; however, it is based on the semi-crystalline nature of elastomeric polypropylene. Because of the viscoelastic properties of the amorphous polypropylene which serves as a soft matrix for the crystals, the effective stiffness of each crystal sensed by the tip is lowered.[47] These observations suggest that there is nearly no measurable rate-dependency of the elastic modulus of either crystalline or amorphous polypropylene in the elastomeric configuration because different types of application modes with different rates, *i.e.* static force distance measurements (1 Hz),[47] peak-force tapping (2 kHz)[47] and bimodal CA-FM-FM-AFM (several MHz) used in this study lead to similar elasticity values. However, there might be a distinctive dependency of the viscoelastic and dissipative properties of the specimen on the shear rate, which needs to be clarified in further investigations.

Conclusions

We have demonstrated that small cantilevers allow for gentle imaging forces ≤10 pN and that a lateral resolution better than 15 nm could be achieved on a semi-crystalline polypropylene during bimodal frequency operation. The image contrast originates from the interactions of the tip with the crystalline and amorphous regions of the polypropylene polymer as quantified by Holscher's approach[38,39] using the data obtained by spectroscopy experiments. The excitation of a second eigenmode free amplitude of 2.0 nm did not affect the frequency shift of the first eigenmode. The amplitudes and frequency shifts for both eigenmodes were recorded approaching the oscillating cantilever on the crystalline and the amorphous regions; this allowed us to estimate the respective elasticities, $E_{\text{eff,cr}} \approx$ 600 MPa and $E_{\text{eff,am}} \approx 300$ MPa. Here, we used single dynamic force curves measured on the distinctive regions of the polymer. However, this approach can be extended to map the local distribution of the elasticity. The results proved that small cantilevers can be used for frequency-modulated AFM in bimodal excitation and that the data can be analysed with

well-established procedures. Further improvements to the electronics of the system would lead to bimodal frequency-modulated high-speed AFM with high data acquisition rates, high lateral resolution and accuracy capabilities, and the ability to record quantitative data.

Acknowledgements

The authors gratefully acknowledge Elena T. Herruzo and Amir Farokh Payam from the Instituto de Ciencia de Materiales de Madrid for fruitful discussions. We also thank the Center of Smart Interfaces for financial support.

References

1 S. N. Magonov, V. Elings and M. H. Whangbo, *Surf. Sci.*, 1997, **375**, L385–L391.
2 R. Garcia and R. Perez, *Surf. Sci. Rep.*, 2002, **47**, 197–301.
3 R. Garcia, *Amplitude Modulation Atomic Force Microscopy*, WILEY-VCH, Weinheim, 2010.
4 T. R. Albrecht, P. Grutter, D. Horne and D. Rugar, *J. Appl. Phys.*, 1991, **69**, 668–673.
5 D. A. Walters, M. Viani, G. T. Paloczi, T. E. Schaffer, J. P. Cleveland, M. A. Wendman, G. Gurley, V. Elings and P. K. Hansma, *Proc. SPIE-Int. Soc. Opt. Eng.*, 1997, **3009**, 43–47.
6 M. B. Viani, T. E. Schaffer, A. Chand, M. Rief, H. E. Gaub and P. K. Hansma, *J. Appl. Phys.*, 1999, **86**, 2258–2262.
7 G. E. Fantner, G. Schitter, J. H. Kindt, T. Ivanov, K. Ivanova, R. Patel, N. Holten-Andersen, J. Adams, P. J. Thurner, I. W. Rangelow and P. K. Hansma, *Ultramicroscopy*, 2006, **106**, 881–887.
8 P. K. Hansma, G. Schitter, G. E. Fantner and C. Prater, *Science*, 2006, **314**, 601–602.
9 C. Braunsmann and T. E. Schaeffer, *Nanotechnology*, 2010, **21**, 225705.
10 M. Leitner, G. E. Fantner, E. J. Fantner, K. Ivanova, T. Ivanov, I. Rangelow, A. Ebner, M. Rangl, J. Tang and P. Hinterdorfer, *Micron*, 2012, **43**, 1399–1407.
11 C. Braunsmann, V. Prucker and T. E. Schaeffer, *Appl. Phys. Lett.*, 2014, **104**, 103101.
12 C. Braunsmann, J. Seifert, J. Rheinlaender and T. E. Schaeffer, *Rev. Sci. Instrum.*, 2014, **85**, 073703.
13 T. Ando, N. Kodera, E. Takai, D. Maruyama, K. Saito and A. Toda, *Proc. Natl. Acad. Sci. U. S. A.*, 2001, **98**, 12468–12472.
14 T. Ando, T. Uchihashi and S. Scheuring, *Chem. Rev.*, 2014, **114**, 3120–3188.
15 T. Fukuma, K. Onishi, N. Kobayashi, A. Matsuki and H. Asakawa, *Nanotechnology*, 2012, **23**, 135706.
16 R. W. Stark, *Mater. Today*, 2010, **13**, 24–32.
17 S. Patil, N. F. Martinez, J. R. Lozano and R. Garcia, *J. Mol. Recognit.*, 2007, **20**, 516–523.
18 C. Dietz, M. Zerson, C. Riesch, A. M. Gigler, R. W. Stark, N. Rehse and R. Magerle, *Appl. Phys. Lett.*, 2008, **92**, 143107.
19 N. F. Martinez, J. R. Lozano, E. T. Herruzo, F. Garcia, C. Richter, T. Sulzbach and R. Garcia, *Nanotechnology*, 2008, **19**, 384011.
20 C. Dietz, E. T. Herruzo, J. R. Lozano and R. Garcia, *Nanotechnology*, 2011, **22**, 125708.
21 D. Kiracofe, A. Raman and D. Yablon, *Beilstein J. Nanotechnol.*, 2013, **4**, 385–393.
22 S. Kawai, T. Glatzel, S. Koch, B. Such, A. Baratoff and E. Meyer, *Phys. Rev. Lett.*, 2009, **103**, 220801.
23 S. Kawai, T. Glatzel, S. Koch, B. Such, A. Baratoff and E. Meyer, *Phys. Rev. B: Condens. Matter*, 2010, **81**, 085420.
24 D. Platz, D. Forchheimer, E. A. Tholen and D. B. Haviland, *Nat. Commun.*, 2013, **4**, 1360.
25 S. S. Borysov, D. Platz, A. S. de Wijn, D. Forchheimer, E. A. Tolen, A. V. Balatsky and D. B. Haviland, *Phys. Rev. B: Condens. Matter*, 2013, **88**, 115405.
26 S. Jesse, S. V. Kalinin, R. Proksch, A. P. Baddorf and B. J. Rodriguez, *Nanotechnology*, 2007, **18**, 435503.
27 D. Platz, E. A. Tholen, D. Pesen and D. B. Haviland, *Appl. Phys. Lett.*, 2008, **92**, 153106.
28 S. D. Solares and G. Chawla, *J. Appl. Phys.*, 2010, **108**, 054901.
29 P. Vitry, E. Bourillot, C. Plassard, Y. Lacroute, L. Tetard and E. Lesniewska, *Appl. Phys. Lett.*, 2014, **105**, 053110.
30 A. Raman, S. Trigueros, A. Cartagena, A. P. Z. Stevenson, M. Susilo, E. Nauman and S. A. Contera, *Nat. Nanotechnol.*, 2011, **6**, 809–814.
31 S. Santos, *Appl. Phys. Lett.*, 2014, **104**, 143109.
32 T. R. Rodriguez and R. Garcia, *Appl. Phys. Lett.*, 2004, **84**, 449–451.
33 E. T. Herruzo, A. P. Perrino and R. Garcia, *Nat. Commun.*, 2014, **5**, 3126.
34 D. Martinez-Martin, E. T. Herruzo, C. Dietz, J. Gomez-Herrero and R. Garcia, *Phys. Rev. Lett.*, 2011, **106**, 198101.
35 F. J. Giessibl, *Science*, 1995, **267**, 68–71.
36 F. J. Giessibl, *Appl. Phys. Lett.*, 2000, **76**, 1470–1472.
37 E. T. Herruzo and R. Garcia, *Beilstein J. Nanotechnol.*, 2012, **3**, 198–206.
38 H. Holscher, B. Gotsmann and A. Schirmeisen, *Phys. Rev. B: Condens. Matter*, 2003, **68**, 153401.
39 H. Holscher and B. Anczykowski, *Surf. Sci.*, 2005, **579**, 21–26.
40 H. J. Butt and M. Jaschke, *Nanotechnology*, 1995, **6**, 1–7.
41 J. R. Lozano, D. Kiracofe, J. Melcher, R. Garcia and A. Raman, *Nanotechnology*, 2010, **21**, 465502.
42 T. R. Albrecht, S. Akamine, T. E. Carver and C. F. Quate, *J. Vac. Sci. Technol., A*, 1990, **8**, 3386–3396.
43 M. B. Viani, T. E. Schaffer, G. T. Paloczi, L. I. Pietrasanta, B. L. Smith, J. B. Thompson, M. Richter, M. Rief, H. E. Gaub, K. W. Plaxco, A. N. Cleland, H. G. Hansma and P. K. Hansma, *Rev. Sci. Instrum.*, 1999, **70**, 4300–4303.

44 N. Rehse, S. Marr, S. Scherdel and R. Magerle, *Adv. Mater.*, 2005, **17**, 2203–2206.
45 A. Sakai, K. Tanaka, Y. Fujii, T. Nagamura and T. Kajiyama, *Polymer*, 2005, **46**, 429–437.
46 C. Dietz, M. Zerson, C. Riesch, M. Franke and R. Magerle, *Macromolecules*, 2008, **41**, 9259–9266.
47 A. Voss, R. W. Stark and C. Dietz, *Macromolecules*, 2014, **47**, 5236–5245.
48 R. Garcia, C. J. Gomez, N. F. Martinez, S. Patil, C. Dietz and R. Magerle, *Phys. Rev. Lett.*, 2006, **97**, 016103.
49 D. H. Gracias and G. A. Somorjai, *Macromolecules*, 1998, **31**, 1269–1276.